

FEATURED ARTICLE

Modeling autosomal dominant Alzheimer's disease with machine learning

Patrick H. Lockett¹ | Austin McCullough¹ | Brian A. Gordon¹ | Jeremy Strain¹ | Shaney Flores¹ | Aylin Dincer¹ | John McCarthy¹ | Todd Kuffner¹ | Ari Stern¹ | Karin L. Meeker¹ | Sarah B. Berman² | Jasmeer P. Chhatwal³ | Carlos Cruchaga¹ | Anne M. Fagan¹ | Martin R. Farlow⁴ | Nick C. Fox⁵ | Mathias Jucker⁶ | Johannes Levin^{7,8,9} | Colin L. Masters¹⁰ | Hiroshi Mori¹¹ | James M. Noble¹² | Stephen Salloway¹³ | Peter R. Schofield^{14,15} | Adam M. Brickman¹⁶ | William S. Brooks^{14,15} | David M. Cash⁵ | Michael J. Fulham^{17,18} | Bernardino Ghetti⁴ | Clifford R. Jack Jr.¹⁹ | Jonathan Vöglein^{8,23} | William Klunk² | Robert Koeppe²⁰ | Hwamee Oh¹³ | Yi Su²¹ | Michael Weiner²² | Qing Wang¹ | Laura Swisher¹ | Dan Marcus¹ | Deborah Koudelis¹ | Nelly Joseph-Mathurin¹ | Lisa Cash¹ | Russ Hornbeck¹ | Chengjie Xiong¹ | Richard J. Perrin¹ | Celeste M. Karch¹ | Jason Hassenstab¹ | Eric McDade¹ | John C. Morris¹ | Tammie L.S. Benzinger¹ | Randall J. Bateman¹ | Beau M. Ances¹ | for the Dominantly Inherited Alzheimer Network (DIAN)

¹ Washington University in St. Louis, St. Louis, Missouri, USA² University of Pittsburgh, Pittsburgh, Pennsylvania, USA³ Brigham and Women's Hospital, Massachusetts General Hospital, Boston, Massachusetts, USA⁴ Indiana University, Bloomington, Indiana, USA⁵ Dementia Research Centre, UCL Queen Square Institute of Neurology, London, UK⁶ German Center for Neurodegenerative Disease, Tübingen, Germany⁷ Ludwig Maximilian University of Munich, Munich, Germany⁸ German Center for Neurodegenerative Diseases, Munich, Germany⁹ Munich Cluster for Systems Neurology (SyNergy), Munich, Germany¹⁰ Florey Institute, The University of Melbourne, Parkville, VIC, Australia¹¹ Osaka City University, Sumiyoshi Ward, Osaka, Japan¹² Taub Institute for Research on Alzheimer's Disease and the Aging Brain, G.H. Sergievsky Center and Department of Neurology, Columbia University Irving Medical Center, New York, New York, USA¹³ Brown University, Providence, Rhode Island, USA¹⁴ Neuroscience Research Australia, Randwick, NSW, Australia¹⁵ University of New South Wales, Sydney, NSW, Australia¹⁶ Columbia University, New York, New York, USA¹⁷ Department of Molecular Imaging, Royal Prince Alfred Hospital, Missenden Road, Camperdown, NSW, Australia¹⁸ University of Sydney, Sydney, NSW, Australia¹⁹ Mayo Clinic, Rochester, Minnesota, USA²⁰ University of Michigan, Ann Arbor, Michigan, USA²¹ Banner Alzheimer Institute, Phoenix, Arizona, USA²² University of California, La Jolla, California, USA²³ Department of Neurology, Ludwig-Maximilians-Universität München, München, Germany

Correspondence

Patrick Luckett, Department of Neurology, Washington University School of Medicine, Campus Box 8111, 660 S. Euclid Avenue, St. Louis, MO 63110.
E-mail: luckett.patrick@wustl.edu

Funding information

This research was funded by the National Institutes of Health (NIH; grant numbers K01AG053474, R01AG052550, UFG 032438, UL1TR000448, P30NS098577, R01EB009352, P50AG05131, U01AG042791, U01AG042791-S1 [FNIH and Accelerating Medicines Partnership], R1AG046179); the German Center for Neurodegenerative Diseases (DZNE); the National Institute for Health Research (NIHR) Queen Square Dementia Biomedical Research Centre; and the Medical Research Council Dementias Platform UK (grant numbers MR/L023784/1, MR/009076/1), BrightFocus Foundation A2018817F, Alzheimer Association International Research Grant Program #AARFD-20-681815, NSF DMS 156243, and an anonymous organization.

We acknowledge the support of Fred Simmons and Olga Mohan, the Barnes-Jewish Hospital Foundation, the Charles F. and Joanne Knight Alzheimer Research Initiative, the Hope Center for Neurological Disorders, the Mallinckrodt Institute of Radiology, the Paula and Rodger O. Riney fund, and the Daniel J. Brennan fund. Computations were performed using the facilities of the Washington University Center for High Performance Computing, which were partially funded by the NIH (grant numbers 1S1ORR022984-01A1, 1S10OD018091-01).

Correction added on February 3, 2021, after first online publication: In the initial publication of this article, the following affiliation was omitted for Jonathan Vöglein: "Department of Neurology, Ludwig-Maximilians-Universität München, Germany." This has now been corrected.

1 | INTRODUCTION

Alzheimer's disease (AD) is the most common form of dementia, accounting for 60% to 70% of the 50 million dementia cases worldwide.¹ AD leads to slow cognitive decline, behavioral and psychiatric disorders, and impairments in functional status. Pathological features of AD include the accumulation of amyloid beta ($A\beta$) plaques, neurofibrillary tau tangles, and neuronal/synaptic losses that correspond with atrophy and decreased glucose metabolism.² The most common form of AD occurs in older age and is known as late-onset Alzheimer's disease (LOAD). Autosomal dominant Alzheimer's disease (ADAD) accounts for <1% of all AD cases and is caused by pathogenic mutations in amyloid precursor protein (*APP*), presenilin 1 (*PSEN1*), or presenilin 2 (*PSEN2*) genes that lead to early increases in $A\beta$ deposition in the brain, which, in turn, is hypothesized to initiate a cascade that causes cognitive decline.^{3,4} The age of onset of cognitive impairment in

Abstract

Introduction: Machine learning models were used to discover novel disease trajectories for autosomal dominant Alzheimer's disease.

Methods: Longitudinal structural magnetic resonance imaging, amyloid positron emission tomography (PET), and fluorodeoxyglucose PET were acquired in 131 mutation carriers and 74 non-carriers from the Dominantly Inherited Alzheimer Network; the groups were matched for age, education, sex, and apolipoprotein $\epsilon 4$ (*APOE* $\epsilon 4$). A deep neural network was trained to predict disease progression for each modality. Relief algorithms identified the strongest predictors of mutation status.

Results: The Relief algorithm identified the caudate, cingulate, and precuneus as the strongest predictors among all modalities. The model yielded accurate results for predicting future Pittsburgh compound B ($R^2 = 0.95$), fluorodeoxyglucose ($R^2 = 0.93$), and atrophy ($R^2 = 0.95$) in mutation carriers compared to non-carriers.

Discussion: Results suggest a sigmoidal trajectory for amyloid, a biphasic response for metabolism, and a gradual decrease in volume, with disease progression primarily in subcortical, middle frontal, and posterior parietal regions.

KEYWORDS

autosomal dominant Alzheimer's disease (ADAD), fluorodeoxyglucose (FDG), machine learning, magnetic resonance imaging (MRI), Pittsburgh compound B (PiB)

ADAD mutation carriers (MC) is earlier than LOAD and remains fairly consistent within a family, allowing for calculation of the estimated age of symptom onset (EAO).⁵

Multiple neuroimaging methods have been used to evaluate in vivo changes in the brain due to AD. [¹¹C]Pittsburgh compound B (PiB) has high affinity for $A\beta$ plaques, with distributions similar to those seen at autopsy.⁶ PiB positron emission tomography (PET) has been used in ADAD to identify amyloid deposition, with amyloid deposition identified >20 years prior to EAO in MC.⁷⁻¹⁰

Studies have also shown increases in PiB retention in MC are associated with a worsening cognitive performance, a decrease in glucose metabolism, and a decrease in hippocampal volume.^{7,11}

[¹⁸F]Fluorodeoxyglucose (FDG) uptake reflects glucose metabolism and has shown promise in discriminating symptomatic MCs from cognitively normal, mutation-negative non-carriers (NC).^{6,9,10} In ADAD, studies have shown FDG uptake in MCs is decreased in the precuneus

RESEARCH IN CONTEXT

- 1. Systematic review:** The authors reviewed the literature using traditional (eg, PubMed) sources and meeting abstracts and presentations. Relevant citations are included where appropriate.
- 2. Interpretation:** Our findings suggest that within autosomal dominant Alzheimer's disease (AD) mutation carriers, amyloid accumulation shows a sigmoidal progression, glucose metabolism shows a biphasic response, and there is a gradual decrease in brain volume, with disease progression primarily in subcortical, middle frontal, and posterior parietal regions. These results are consistent with clinical findings.
- 3. Future directions:** Future work will focus on (a) understanding the role of increased glucose metabolism observed in the early stages of the disease; (b) relating the current results with other functional neuroimaging methods, such as cerebral blood flow and resting state functional magnetic resonance imaging; and (c) relating the current results with blood and cerebrospinal fluid biomarkers of AD.

and is inversely correlated with PiB binding. Marked decreases in glucose metabolism occur approximately 5 to 10 years before EAO in MCs.^{10,12}

Structural magnetic resonance imaging (MRI) provides a method to evaluate regional volumetric changes in neurodegeneration that occur with disease progression.¹³ MRI can reveal regional brain atrophy, which is a characteristic feature of neurodegeneration due to synaptic losses.¹⁴ ADAD is characterized by progressive atrophy that manifests as changes initially in the temporal lobes and subcortical regions with eventual spread to other regions. Observed changes in atrophy are related to the spread of neurofibrillary tangles in AD.¹⁴

Machine learning (ML) is a branch of artificial intelligence that can learn to extract patterns from existing data to predict future events.¹⁵ Advances in ML offer promise for a number of applications, including medical imaging and predictive analytics.^{15,16} Compared to traditional statistics that provide primarily group-level results, ML algorithms can predict clinical outcomes at the individual level and could enable personalized treatments that provide targeted care for patients.¹⁷ Although a number of studies have applied ML to neuroimaging measures to study LOAD,^{18–22} few studies to date have applied these techniques to ADAD. Because time until conversion to symptomatic impairment can be estimated with EAO, ADAD provides a unique opportunity for ML to model the progression of the disease and provide decision support to evaluate therapies currently being investigated in the Dominantly Inherited Alzheimer Network Trials Unit (DIAN-TU).

In this longitudinal study, we used artificial neural networks (ANNs) to evaluate progression to cognitive impairment using multimodal neuroimaging biomarkers. Specifically, within a cohort of MCs ($n = 131$)

and NCs ($n = 74$), we used ANNs to investigate: (1) changes in A β deposition (using PiB), (2) changes in glucose metabolism (using FDG), and (3) brain atrophy (using structural MRI) as a function of aging in relation to EAO. Further, we used feature selection to identify regions that were the strongest discriminators of mutation status for each modality. We then performed Monte Carlo simulations to identify cut-offs for the identified regions. This data-driven approach provides an opportunity to discover novel mechanisms and disease trajectories specific for ADAD.

2 | METHODS**2.1 | Participants**

One hundred thirty-one MCs with mutations in *PSEN1*, *PSEN2*, or *APP* and 74 healthy, mutation-negative NCs were recruited from sites participating in the DIAN study. Participants from the 12th data freeze with genetic, clinical, and longitudinal neuroimaging data that passed quality control procedures were included. The Washington University Institutional Review Board provided supervisory review and human subjects' approval. Participants provided written, informed consent, or assent with proxy consent. All study procedures were approved by the Washington University Human Research Protection Office and the institutional review boards of the participating sites.

2.2 | Clinical classification

The Clinical Dementia Rating (CDR[®]) Dementia Staging Instrument was used to assess dementia status at each clinical assessment.²³ A participant's EAO was calculated at each visit on the basis of the participant's current age relative to the family mutation-specific expected age at onset of dementia symptoms.⁵ Parental age at first progressive cognitive decline was used if the mutation-specific EAO was unknown. EAO was calculated identically for both MCs and NCs. All clinical evaluators were blinded to the mutation status of participants. The presence/absence and type of mutation were determined using polymerase chain reaction amplification followed by Sanger sequencing.⁷

2.3 | MRI acquisition and processing

MRI was performed using the Alzheimer's Disease Neuroimaging Initiative (ADNI) protocol.²⁴ Sites used a 3T scanner that passed regular quality control assessments. The ADNI Imaging Core screened images for compliance. T1 weighted images at $1.1 \times 1.1 \times 1.2$ mm voxel resolution were acquired for participants. FreeSurfer 5.3^{25,26} was used to perform volumetric segmentation, cortical surface reconstruction, and to define cortical and subcortical regions of interest (ROIs). Segmentations were inspected and edited as needed by members of the DIAN Imaging Core. A regression approach was used to correct subcortical volumes for intracranial volumes. Volumetric measures were averaged across hemispheres. FreeSurfer-defined cortical and subcortical ROIs (44 total) were used for regional processing of PET data. The FreeSurfer-defined ROIs were derived from the Desikan/Killiany

atlas²⁷ for segmentation. These are standard regions used for volumetric analyses.

2.4 | PET acquisition and processing

Amyloid PET was performed using a bolus injection of PiB. Data from 40 to 70 minutes post-injection were converted to regional standardized uptake value ratios (SUVRs) relative to the cerebellar gray matter using FreeSurfer-derived ROIs (PET Unified Pipeline).²⁸ Glucose metabolism imaging was performed with a single bolus injection of FDG. A 30-minute dynamic acquisition beginning 30 minutes post-injection was acquired. The last 20 minutes of each FDG scan were converted to SUVRs using the cerebellar gray matter as a reference region. All PET data were partial volume corrected using a regional spread function technique.^{29,30} PET images were aligned to the T1 image processed using FreeSurfer. PET scanner-specific filters were applied to account for differences in spatial resolution and to achieve a common resolution (8 mm).³¹ The DIAN imaging core performed quality control checks on the PET Unified Pipeline processing.

2.5 | Machine learning and statistical analyses

ML analyses were performed in MATLAB R2018b. Deep feedforward ANNs were trained for each of the neuroimaging modalities. Feedforward ANNs map an input to an output by composing sets of smaller functions laid out as a directed acyclic graph.³² The feasibility of these networks is based on the universal approximation theorem, which states a neural network with a single hidden layer contains a finite set of artificial neurons that approximate continuous functions on subsets of \mathbb{R}^n .³³

Our ANNs contained four hidden layers with 10 artificial neurons in each layer. The network architecture was decided based on design methodologies,^{34,35} incremental pruning, and cross-validation. Further details on model design and validation can be found in supporting information (Methods—Machine Learning Model Design). An ANN was trained to output all ROIs for each modality. Input to the models included age, sex, apolipoprotein E (APOE) $\epsilon 4$ status, mutation status, the amount of time in the future to predict, and the given imaging variables (MRI or SUVR) for 44 FreeSurfer ROIs. A complete list of the ROIs can be found in Table S1 in supporting information. The output of each model corresponded to the ROI values at a time point in the future. Rates of change were calculated by subtracting scans at time point N by the scan at time point $N-1$. Rates were then divided by the number of months between the scans to obtain a normalized rate of change. The mean time between scans was 2.6 years (± 1.4). If a participant had more than two scanning sessions, all possible combinations were evaluated. Using the first time point, data were projected into the future by iteratively adding the normalized rate of change, and these data were used for training. For each point, the rate of change was used to project the data ± 3 years from the current age. Data were projected into the future and the past to avoid biasing the model to later phases of the disease. We chose this window based on previous work,¹⁰ which showed

the biomarkers' rate of change is not constant along the disease continuum.

Predictive features of mutation status were ranked according to importance using a Relief algorithm.³⁶ Relief algorithms detect conditional dependencies between attributes using a nearest neighbor approach, with features ranked by estimating how well their values distinguish between proximal comparisons. Further, cutoff points for PiB, FDG, and brain volumetrics were identified based on the likelihood of the values generated by Monte Carlo model simulations. The simulations generated an equal number (by mutation status) of random sample points from the multivariate distribution defined by the mean and covariance matrix of the data given a specific mutation status, age, and EAO range.³⁷

We also trained a linear regression model to compare the results to our ANN. This comparative analysis was performed due to recent research suggesting that, in some cases, linear models can outperform nonlinear models.³⁸ When training the regression model, all methods previously described for training the ANN were applied. Each biomarker was modeled separately, and the models were trained using five-fold cross-validation. Cross-validation was performed at the participant level, and all results reported were derived by combining the test data results from each of the five folds of cross-validation. In addition, the input to the regression model was the same as the ANN, but the only output considered was the precuneus. We chose the precuneus as it is highly predictive and heavily involved in disease progression in ADAD,¹⁰ making it optimal for comparison. Further, a multivariate linear regression was performed that derived brain regions in the same manner as the ANN. The regression model used ordinary multivariate normal maximum likelihood estimation with the full variance-covariance matrix and constant, linear, and interaction terms. We also performed the zero-rule algorithm on the data to compare baseline predictability using the mean of the output values observed in the training data compared to the testing data.

3 | RESULTS

3.1 | Demographics of the cohort

Detailed demographics are presented in Table 1. Participants were matched for age, sex, and education.

3.2 | PiB

The Relief algorithm identified the nucleus accumbens, caudate, precuneus, anterior cingulate, pallidum, putamen, and middle frontal regions as strong predictors of mutation status. The ANN was able to predict the future PiB values with an average R^2 value of 0.95 and root mean square error (RMSE) of 0.2. Figure 1 depicts results for the four best-predicted ROIs. The algorithm was able to accurately estimate the values in both MCs and NCs, with the NCs having lower SUVRs compared to the MCs. Figure S1 in supporting information shows the model predictions for MCs based on distance from EAO for PiB. Two relatively

TABLE 1 Demographics of participants

	Mutation carriers (MC)	Mutation-negative non-carriers (NC)	P values
N	131	74	
Age (years) ± SD	39.2 ± 10.6	39.3 ± 10.2	.95
Sex (% male)	40%	35%	.72
Education (years) ± SD	14.3 ± 2.7	15.1 ± 2.6	.06
APOE ε4 (% carriers)	39%	36%	.81
EAO (years) ± SD	46.3 ± 6.8	48.1 ± 5.7	.90

APOE ε4 = apolipoprotein ε4; EAO = estimated age of symptom onset; SD = standard deviation.

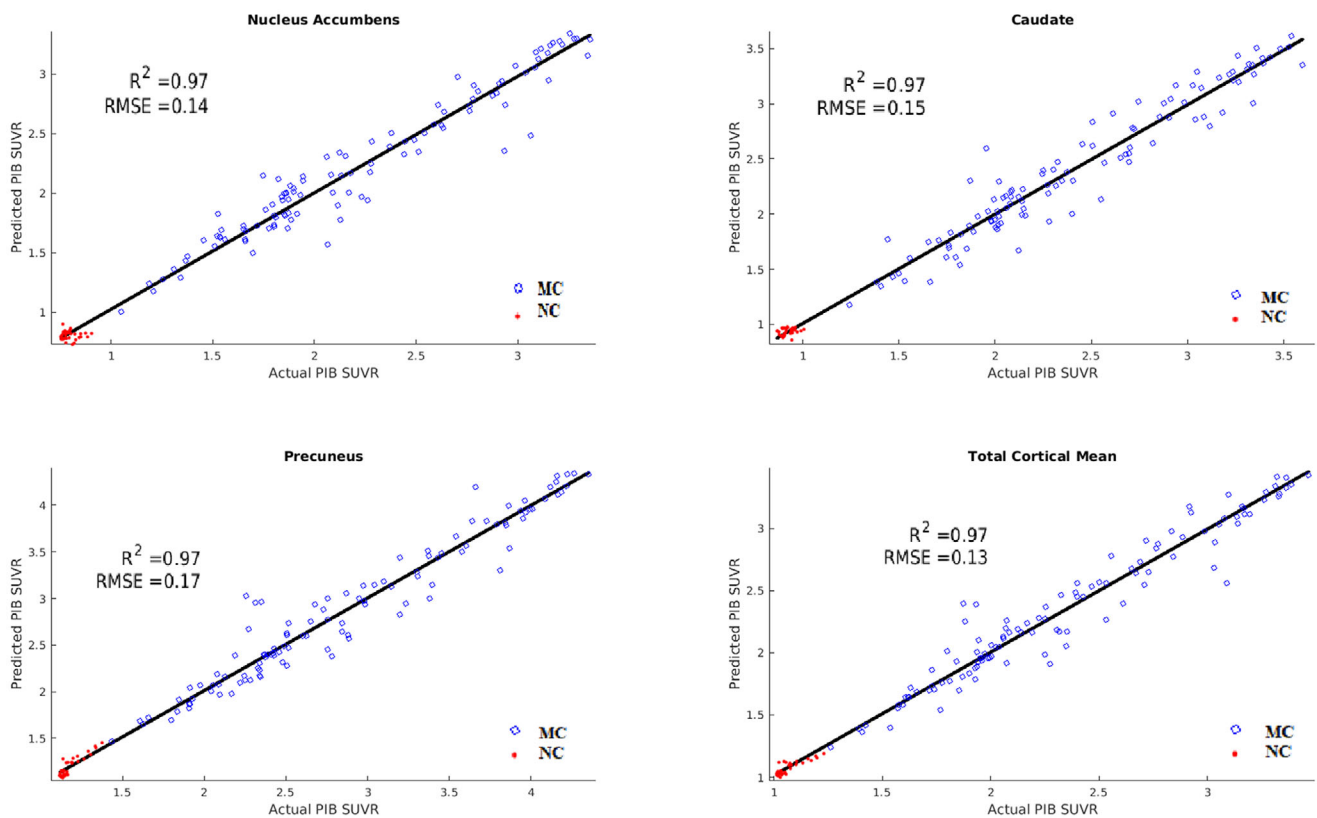


FIGURE 1 Results of Pittsburgh compound B (PiB) predictions for mutation carriers (MC; blue) and non-carriers (NC; red). Correlation and root mean squared error (RMSE) of predicted versus actual values. The artificial neural network (ANN) was able to predict future PiB values with an average R^2 of 0.95 and RMSE of 0.2 in both MCs and NCs. SUVR, standardized uptake value ratio

distinct clouds were seen for PiB, with lower SUVRs seen at greater distances from EAO, while MCs closer to EAO had elevated PiB SUVRs.

3.3 | FDG

The strongest predictors of mutation status with respect to metabolism were the pericalcarine, caudate, precuneus, fusiform, anterior cingulate, insula, and transverse temporal regions. The ANN was able to predict future FDG values with an R^2 value of 0.93 and RMSE of 0.02 in both groups. Figure 2 depicts results for the four

best-predicted ROIs. The algorithm showed a trend of MCs having lower future FDG values than NCs. Figure S2 in supporting information shows the model predictions for MCs based on distance from EAO for FDG. Two clouds are seen for FDG, with higher SUVRs seen at greater distances from EAO, while MCs closer to EAO had lower FDG SUVRs.

3.4 | Volume

The strongest predictors of mutation status with respect to brain atrophy were seen in the nucleus accumbens, pericalcarine, caudate,

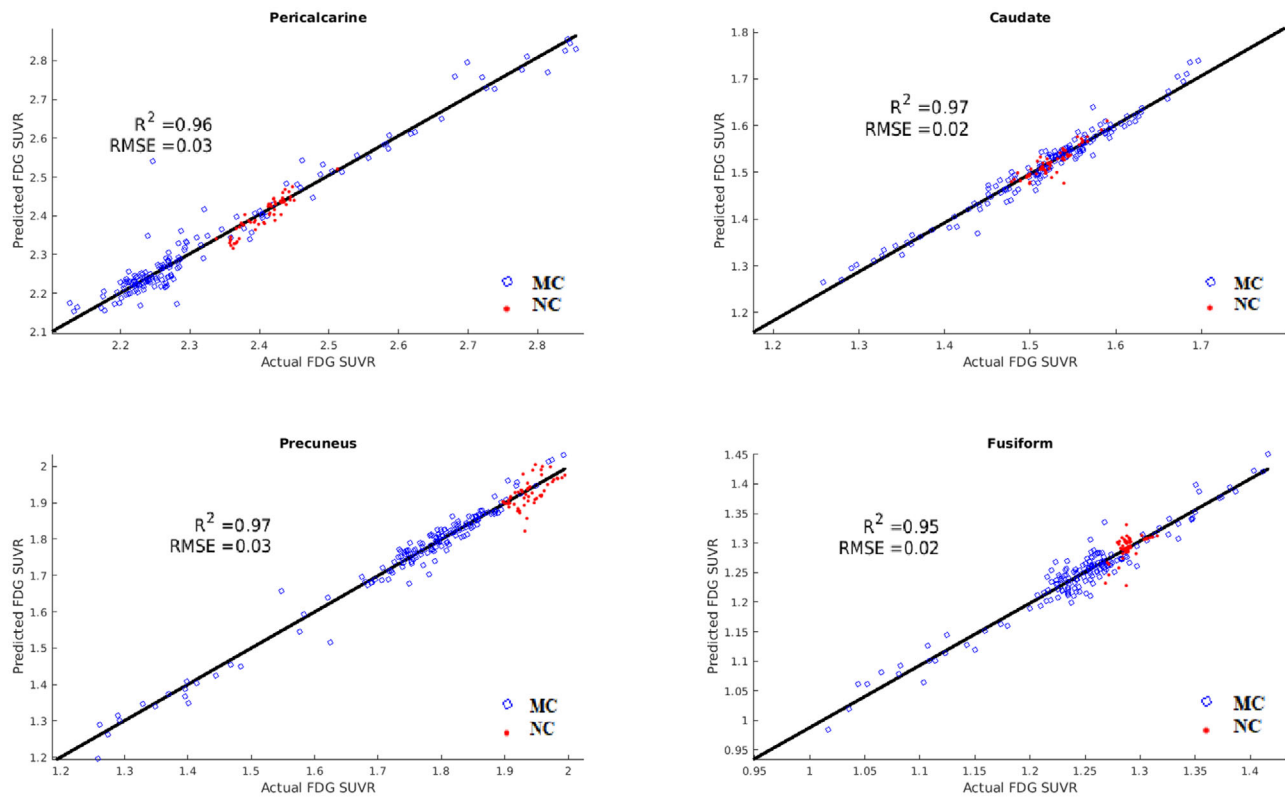


FIGURE 2 Results of fluorodeoxyglucose (FDG) predictions for mutation carriers (MC; blue) and non-carriers (NC; red) in select regions of interest. Correlation and root mean squared error (RMSE) of predicted versus actual values. The ANN was able to predict future FDG values with an average R^2 of 0.93 and RMSE of 0.02 in MCs and NCs, with MCs showing trends of lower predicted FDG values than NCs. SUVR, standardized uptake value ratio

precuneus, anterior cingulate, insula, entorhinal cortex, pallidum, and transverse temporal regions. The ANN was able to predict changes in brain volumes with an average R^2 value of 0.95. Figure 3 depicts results for the four best-predicted regions. The algorithm showed a general trend of MCs having more brain atrophy than NCs. Figure S3 in supporting information shows the model predictions for MCs as a function of distance from EAO for brain volumes.

3.5 | Simulations

Using the trained models, amyloid accumulation, changes in metabolism, and brain atrophy were simulated for MCs and NCs (Figure 4, top). Consistent with previous work, the models showed that in the MC group, the earliest changes are in amyloid deposition, which follows a sigmoidal trajectory and continues to accumulate past EAO. A biphasic response was seen for metabolism, with changes occurring earlier than expected, and progressive decline was observed in atrophy throughout the course of the disease, with the greatest changes occurring just prior to EAO. The NC groups showed little change over time for all modalities.

We fitted a polynomial curve to the normalized rates of change for each of the neuroimaging biomarkers (Figure 4, bottom left). Consistent with the models, amyloid showed an inverted *U* shape, with

increases occurring early in the disease, and subsequently followed by a gradual decline in rate of PiB accumulation. FDG showed a slight increase in the early stages, followed by a gradual decrease when the distance from EAO approached 0. Finally, brain volumetrics showed a gradual increase in the rate of decline throughout progression to EAO.

Figure 4 (bottom right) shows the normalized model errors based on years to predict (eg, the error for a participant's PET/MRI values predicted 1 year in the future vs the error for predicting 5 years in the future). A two-degree polynomial curve was fit to the error data, which showed a predominantly linear increase with increasing number of years to predict. The fit lines were projected into the future for up to 40 years. The plot shows that the model maintains a mean absolute error <0.1 up to 10 years in the future. The individual biomarkers showed similar trends, only at different scales.

Figures S4–S6 in supporting information display the results of the Monte Carlo model simulations for each of the highly predictive regions for each modality. Larger values on the y-axis represent a greater likelihood of producing a given value. For PiB, clear cut-points were observed between MCs and NCs with nearly 100% specificity. Cut-points were 1.17 for the nucleus accumbens, 1.3 for the caudate, 1.4 for the precuneus, and 1.2 SUVR for total cortical mean. For FDG, the cut-points were less defined for some regions. Cut-points for the anterior cingulate, caudate, precuneus, and total cortical mean ranged

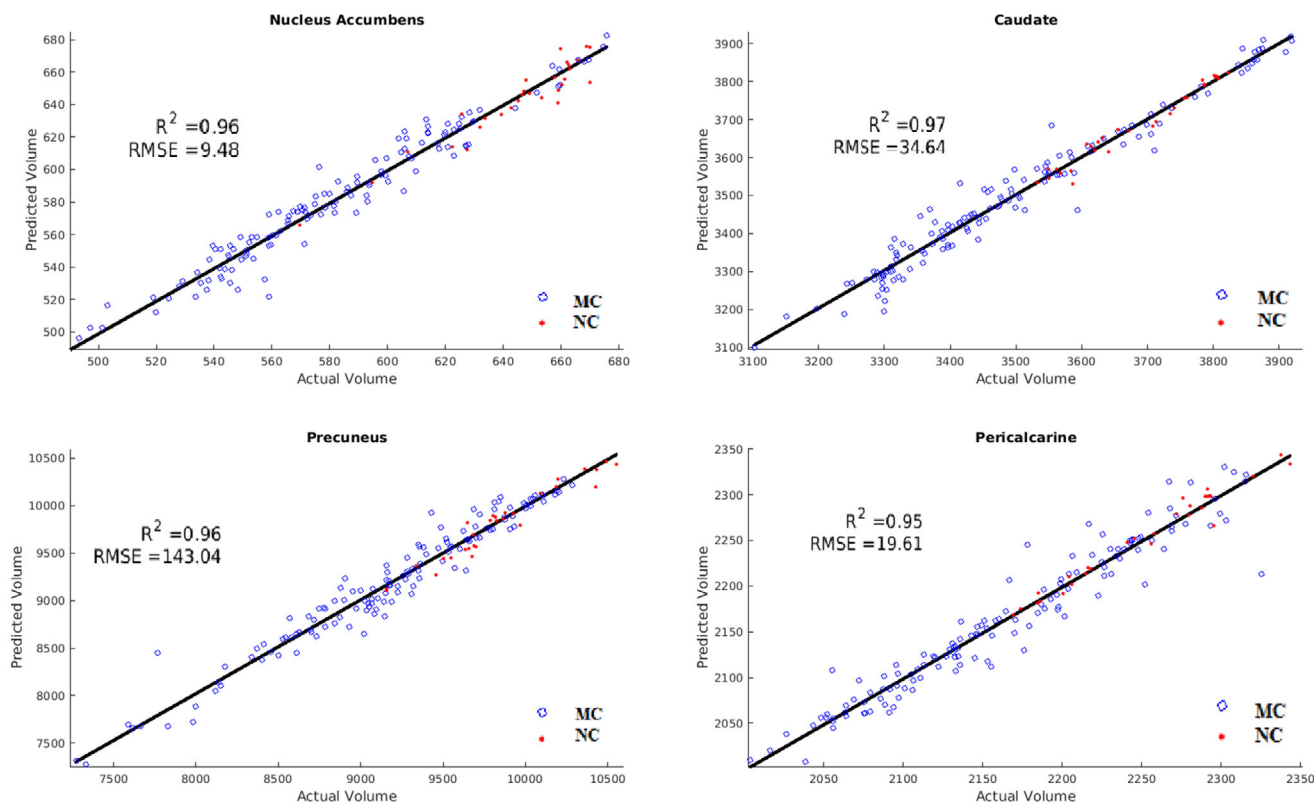


FIGURE 3 Results of brain volumetric predictions for mutation carriers (MC; blue) and non-carriers (NC; red). Correlation and root mean squared error (RMSE) of predicted versus actual values. The artificial neural network (ANN) was able to predict changes in brain volumes with an average R^2 value of 0.95 and showed a general trend of MCs having more brain atrophy than NCs

from 1.4 to 1.825 SUVR. The model simulations indicate MCs had a trend for decreased FDG in each of these ROIs, as well as a biphasic response in the caudate and anterior cingulate. For brain volumes, MCs had greater atrophy than NCs. Cutoffs were identified for the nucleus accumbens (550 mm^3), caudate (3300 mm^3), precuneus (8500 mm^3), and total gray matter ($575,000 \text{ mm}^3$).

3.6 | Alternative analysis methods

Figure S8 in supporting information displays the error histograms (probabilities of errors [actual-predicted]) for the ANN versus the regression model for PiB in the precuneus. Although both models performed very well, the performance obtained through regression was lower than that obtained through the ANN. The ANN's error probability distribution was highly clustered around 0 (RMSE = 0.17), whereas the regression model showed greater dispersion (RMSE = 0.28), indicating a greater likelihood of making a larger error compared to the ANN. Similar results were seen using FDG and volumetric data. Whole brain average RMSE for the ANN, multivariate linear regression, and zero-rule algorithm are provided at the bottom of Table S1. As expected, the ANN showed lower RMSE compared to multivariate linear regression and the zero-rule algorithm for all modalities.

4 | DISCUSSION

Our models yielded high accuracy in predicting amyloid accumulation, changes in metabolism, and brain atrophy in ADAD. The Relief algorithm identified both subcortical (caudate) and cortical (precuneus and anterior cingulate) ROIs as the strongest predictors of mutation status. Figure 5 displays the strongest predictors for each modality. For amyloid PET, which is believed to reflect the earliest changes in ADAD, changes were primarily seen within subcortical (pallidum, nucleus accumbens, caudate, putamen, and entorhinal) compared to cortical regions (middle frontal, anterior cingulate, and precuneus). For changes in metabolism measured by FDG, which reflect changes later in the disease process compared to amyloid, more cortical (insula, fusiform, middle frontal, precuneus, anterior cingulate, pericalcarine, and transverse temporal) rather than subcortical (caudate) regions were involved.

For changes that occur late in the disease process due to atrophy, both cortical (precuneus, anterior cingulate, pericalcarine, transverse temporal) and subcortical (caudate, pallidum, nucleus accumbens, entorhinal, thalamus) regions were affected. This suggests that the disease may start within subcortical areas and quickly involve additional subcortical and cortical regions. Overall, these analyses point to multiple hubs being affected early in the disease process, followed by spread to other brain regions (Figure S7 in supporting information). Table S1 lists the RMSE for the individual ROIs for each of the three

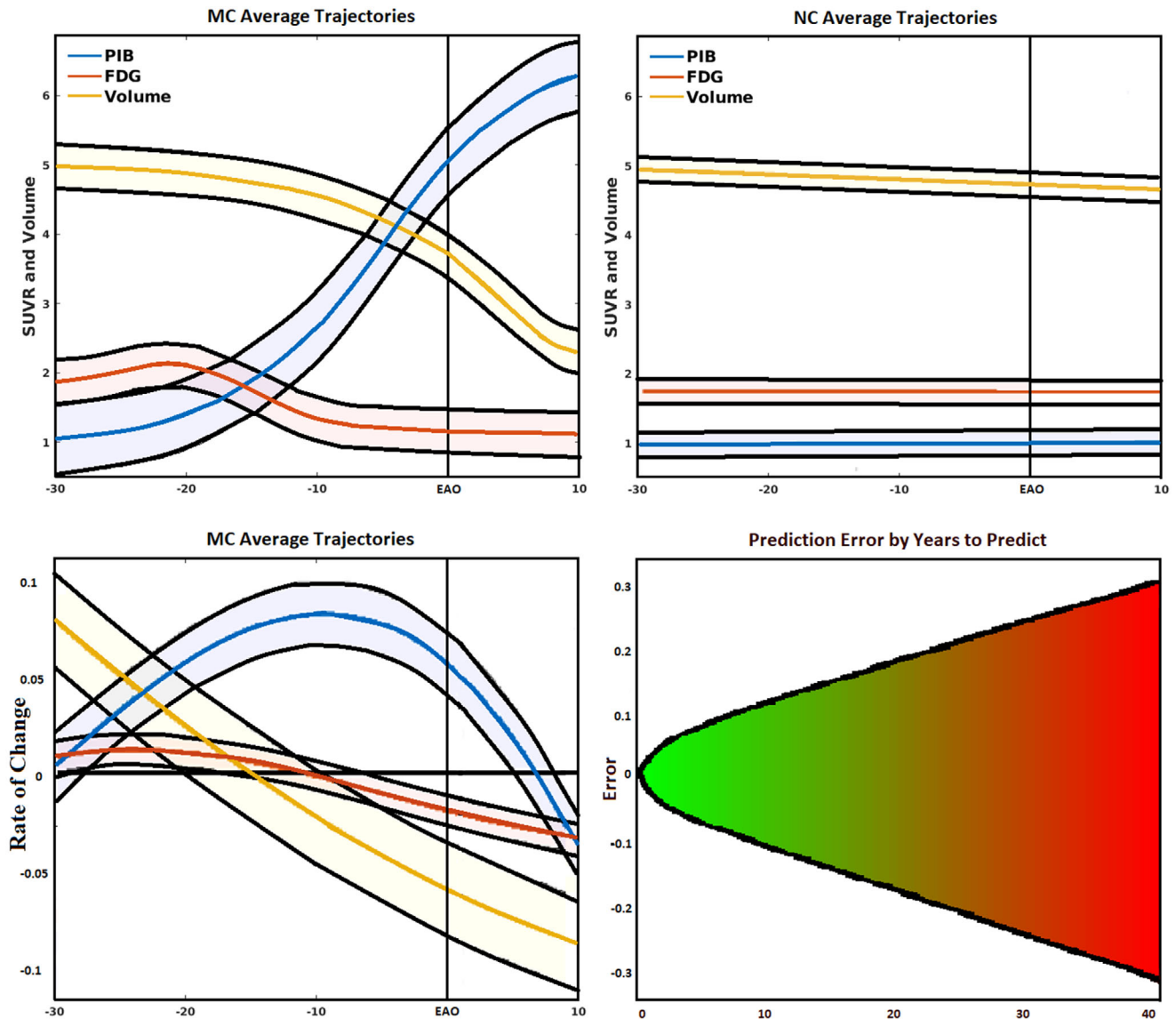


FIGURE 4 Top left, Simulated biomarker evolution for total mean cortical and subcortical Pittsburgh compound B (PiB), total mean cortical and subcortical fluorodeoxyglucose (FDG), and total gray matter volume (scaled to a common interval) derived from the artificial neural network (ANN) in mutation carriers (MC). Shaded region indicates model variability, with estimated age of onset (EAO) marked by perpendicular line. Top right, Simulated biomarker evolution for total mean cortical and subcortical PiB, total mean cortical and subcortical FDG, and total gray matter volume (scaled to a common interval) derived from the ANN in mutation non-carriers (NC). Bottom left, Normalized biomarker rate of change for mean PiB, mean FDG, and total gray matter volume (scaled to a common interval) fit to a polynomial curve showing 95% confidence interval. Bottom right, Mean absolute error of predicted (normalized) biomarker values given the amount of time in the future to predict, fit with a two-degree polynomial curve projected into the future. Errors increased linearly with an increase in the amount of time in the future to predict. SUVR, standardized uptake value ratio

biomarkers, as well as the mean overall RMSE of the models compared to the zero-rule algorithm and multivariate linear regression.

In the amyloid analysis, the model achieved 0.95 R^2 and 0.2 RMSE (see Figure 1). The model showed PiB uptake was greater in MCs compared to NCs for most regions. Our results also confirm that the presence of amyloid alone is insufficient for conversion to symptomatic AD. The simulated trajectory for mean cortical amyloid accumulation (see Figure 4, top left) showed deposition started to occur approximately 15 to 20 years before EAO. These results are consistent with other studies

that focused on global and regional amyloid deposition.^{7,11} Our model indicates a sigmoidal trajectory of accumulation for amyloid, with a slow increase 20 to 30 years from EAO, an abrupt increase 0 to 15 years from EAO, and slowing to an eventual decline after EAO. This is consistent with what has been hypothesized to occur in LOAD.³⁹

As a point of reference, we calculated the normalized rates of change for all mutation-positive participants (see Figure 4, bottom left). The normalized rate of amyloid deposition shows a consistent increase from roughly 10 years prior to EAO followed by slowing in the rate of

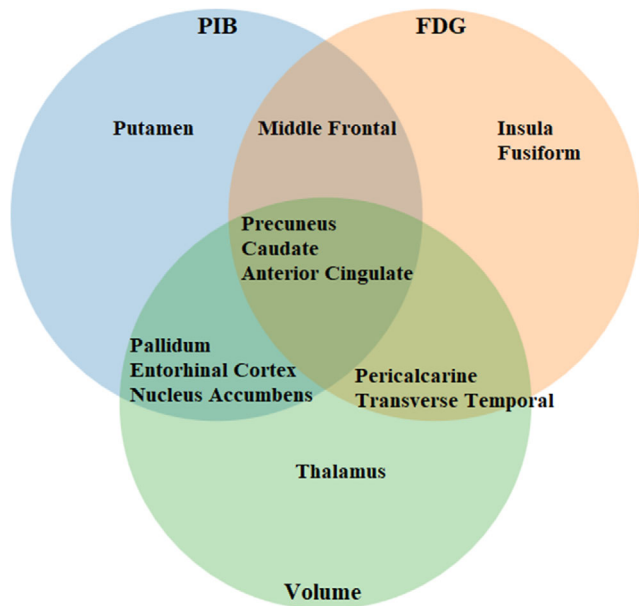


FIGURE 5 Strongest predictors of mutation carrier (MC) status for autosomal dominant Alzheimer's disease (ADAD) as identified by Relief algorithms. The strongest predictors across all modalities were the precuneus, caudate, and anterior cingulate. Changes in amyloid positron emission tomography (Pittsburgh compound B [PiB], blue circle) were primarily seen within subcortical regions. Changes in metabolism (fluorodeoxyglucose [FDG], orange circle) showed more cortical involvement. Volumetric changes (Volume, green circle) showed both cortical and subcortical involvement

accumulation after EAO. Only after EAO does the rate of accumulation diminish, which is consistent with the sigmoidal model trajectory.

With regard to metabolism, our model yielded 0.93 R^2 and 0.02 RMSE. Although the MCs had greater decrease in FDG for most brain regions, the separation between the two groups was not as well defined compared to PiB. This is likely because the rate and amount of change are less extreme compared to amyloid (see Figure 4, top left). Our model indicates metabolism did not decrease below a baseline until 10 years before symptom onset and continued to decline after EAO. These results are consistent with the normalized rate of change (see Figure 4, bottom left). The rate of metabolism did not decline below baseline until 10 years prior to EAO, followed by a steady decline.

An uptick in metabolic activity was observed in the early stages of amyloid accumulation and did not begin to decrease until amyloid significantly increased. This was observed in the simulated trajectory and the normalized rate of change. Similar results were observed within the precuneus in a cross-sectional analysis.⁷ Rate of change analysis revealed this primarily occurs in the basal ganglia. Because the basal ganglia show the least toxic response to amyloid deposition,^{40–42} these transient increases may be prominent because these neurons mount a compensatory response preceding significant amyloid accumulation.^{43–47} However, at some point, the brain is no longer able to buffer changes when amyloid deposition becomes significant.

Our model showed total gray matter volume slightly declined during the early stages of ADAD, followed by a dramatic decrease 5 to

10 years prior to EAO. The decrease in volume occurred when metabolism was decreased and amyloid had accumulated. Volumetrics continued to decline even after EAO. The model was able to predict volumes with an R^2 of 0.95.

These findings have clinical importance for the care of people with ADAD in the context of amyloid, metabolism, and atrophy. Using feature selection methods, we have identified brain regions that are both common among modalities as well as unique for each modality (Figure 5). Specifically, we have shown the precuneus, caudate, and anterior cingulate are strong predictors of mutation status among all modalities. These findings are significant for multimodal imaging studies and clinical trials whose goal is to assess the overall impact of a therapy. Further, the fact that we have identified regions that are unique to each modality suggests a complex set of evolving interactions that are not localized to a small set of brain regions. Our models also suggest a complex disease progression that goes beyond a linear or sigmoidal pattern that has been hypothesized for LOAD (Figure 4). We have identified a biphasic response in metabolism, in which hypermetabolism is seen very early in the disease process. Future studies should investigate this phenomenon, as previous studies have primarily focused on hypometabolism that occurs later in the disease process.

We also extend the literature by establishing clinically useful algorithms for modeling the progression of ADAD, and show the utility of ML in developing diagnostic and predictive tests. A major deficiency in AD clinical research is the problem of individual predictability versus group-level differences. ML is ideal for research aimed at discovering patterns in high-dimensional data that are believed to underlie complex clinical phenotypes that go beyond group-level results. This is especially relevant for diseases such as ADAD and LOAD, which show chronic progression over long periods of time, as well as variability in terms of symptoms, risk factors, and progression. Our models were trained on the largest available ADAD data set, and are able to accurately forecast disease progression several years into the future at any stage of the disease. Inputting a patient's unique demographics and imaging variables will yield trajectories that are specific to that individual. Further, by simulating our trained models, we are able to identify trajectories and cutoff values unique to each brain region that best discriminate MCs from NCs. Because our models have been trained on a variety of demographics, one can easily generate values that are specific to a given sex, APOE $\epsilon 4$ status, and education level. Use of these models provides the opportunity to expedite clinical trials and provide precision medicine tailored to a patient based on his/her unique set of demographics, disease subtype, and treatment response. As we have shown, while both linear regression and our ANN performed well in predicting disease progression, the ANN had a lower error rate. More accurate models could lead to better decision making and improved efficiency of research, and accurate identification of participants whose progression patterns differ from model predictions could allow for decision support in evaluating the effects of specific therapies in clinical trials.

Limitations and future work for this study are detailed as follows. Data leakage, which refers to the use of test data in any part of the training process, is a major concern in the AD field,⁴⁸ and is difficult

to address due to the limited number of samples. This is especially relevant in the context of ADAD. While we use the largest available data set, the fact that ADAD only accounts for a small portion of the total AD cases restricts the number of available of samples. Still, choosing the proper set of hyperparameters in the context of deep neural networks is a difficult task. However, the performance and flexibility of these models crucially depends on how these parameters are set.⁴⁹ In our analysis, the number of layers and number of artificial neurons in each layer were identified by testing multiple network architectures within our data (see supporting information). Measures were taken to ensure that the partitioning of the data for five-fold cross-validation in this process did not match the data partitions used for the five-fold cross-validation for the final analysis. We also ensured the models trained in the network architecture identification process were discarded after the fact, and all subsequent models generated in the main analysis had randomly initialized weights. However, because the same data set was used to identify the size of the network as well to perform the main analysis, we acknowledge that this could be a source of data leakage, which could lead to an underestimation of errors. Future work will involve further validation and testing of the proposed models. Specifically, conducting blinded out-of-sample testing on newly acquired data from the DIAN study is needed to ensure issues such as data leakage and overfitting do not influence the model results. Further, alternative network models will need to be considered. As more longitudinal time points are acquired for participants in DIAN, time series-specific networks, such as long short-term memory network may be more appropriate. Last, alternative forms of feature selection should be considered to investigate the relationships between biomarkers and brain regions.

5 | CONCLUSION

To provide targeted treatment to persons with ADAD, novel methods are needed to model disease trajectories. We have shown ANNs can accurately forecast amyloid accumulation, changes in glucose metabolism, and brain atrophy. Using feature extraction methods, we identified the strongest predictors of mutation status over 44 brain regions. Our results show a sigmoidal progression of amyloid accumulation, a biphasic response to glucose metabolism, and a gradual increase in brain atrophy in MCs compared to NCs. Our models indicate disease progression is primarily in subcortical regions, followed by cortical involvement within anterior and posterior portions of the brain.

ACKNOWLEDGMENTS

We would like to acknowledge the participants and their families, without whom these studies would not be possible. We additionally thank all of the participating researchers and coordinators in the DIAN (<https://dian.wustl.edu/our-research/observational-study/dian-observational-study-sites/>) who support the studies. DIAN ClinicalTrials.gov identifier: NCT00869817.

CONFLICTS OF INTEREST

The authors declare no conflicts of interest. Anne Fagan received research funding from the National Institute on Aging of the National Institutes of Health, Biogen, Centene, Fujirebio, and Roche Diagnostics. She is a member of the scientific advisory boards for Roche Diagnostics, Genentech, and AbbVie and also consults for Araclon/Grifols, DiademRes, DiamiR, and Otsuka. Carlos Cruchaga receives research support from Biogen, EISAI, Alector, and Parabon. The funders of the study had no role in the collection, analysis, or interpretation of data; in the writing of the report; or in the decision to submit the paper for publication. Dr. Cruchaga is also a member of the advisory board of ADx Healthcare, Halia Therapeutics, and Vivid Genomics. Jasmeer P. Chhatwal served on the medical advisory board for Otsuka Pharmaceuticals. Johannes Levin reports speaker's fees from Bayer Vital, speaker's fees from Willi Gross Foundation, consulting fees from Axon Neuroscience, consulting fees from Ionis Pharmaceuticals, author fees from Thieme medical publishers and W. Kohlhammer GmbH medical publishers, compensation for work as part-time CMO from MODAG GmbH, and non-financial support from AbbVie outside the submitted work. John Morris is funded by NIH grants (numbers P50AG005681, P01AG003991, P01AG026276, U01AG032438). Dr. Jack serves on an independent data monitoring board for Roche and has served as a speaker for Eisai, but he receives no personal compensation from any commercial entity. He receives research support from NIH and the Alexander Family Alzheimer Disease Research Professorship of the Mayo Clinic. Eric McDade is involved in a clinical trial on AV-1451 sponsored by Avid and serves on a data safety monitoring committee for Eli Lilly. Randall Bateman is on the scientific advisory board of C2N Diagnostics and reports research support from AbbVie, Biogen, Eisai, Eli Lilly, Co/Avid Radiopharmaceuticals, Roche, Janssen, and United Neuroscience.

REFERENCES

1. World Health Organization. *Dementia fact sheet*. WHO 2017;17:751-760.
2. Serrano-Pozo A, Frosch MP, Masliah E, Hyman BT. Neuropathological alterations in Alzheimer disease. *Cold Spring Harb Perspect Med*. 2011;1:6189.
3. Bateman RJ, Aisen PS, De Strooper B, et al. Autosomal-dominant Alzheimer's disease: a review and proposal for the prevention of Alzheimer's disease. *Alzheimer's Res Ther*. 2011;3:1-13.
4. Schindler SE, Fagan AM. Autosomal dominant Alzheimer disease: a unique resource to study CSF biomarker changes in preclinical AD. *Front Neurol*. 2015;6:142.
5. Ryman DC, Acosta-Baena N, Aisen PS, et al. Symptom onset in autosomal dominant Alzheimer disease: a systematic review and meta-analysis. *Neurology*. 2014;83:253-260.
6. Marcus C, Mena E, Subramaniam RM. Brain PET in the diagnosis of Alzheimer's disease. *Clin Nucl Med*. 2014;39:413.
7. Bateman RJ, Xiong C, Benzinger TLS, et al. Clinical and biomarker changes in dominantly inherited Alzheimer's disease. *N Engl J Med*. 2012;367:795-804.
8. Yau WYW, Tudorascu DL, McDade EM, et al. Longitudinal assessment of neuroimaging and clinical markers in autosomal dominant Alzheimer's disease: a prospective cohort study. *Lancet Neurol*. 2015;14:804-813.

9. McDade E, Wang G, Gordon BA, et al. Longitudinal cognitive and biomarker changes in dominantly inherited Alzheimer disease. *Neurology*. 2018;91:1295-1306.
10. Gordon BA, Blazey TM, Su Y, et al. Spatial patterns of neuroimaging biomarker change in individuals from families with autosomal dominant Alzheimer's disease: a longitudinal study. *Lancet Neurol*. 2018;17:241-250.
11. Oxtoby NP, Young AL, Cash DM, et al. Data-driven models of dominantly-inherited Alzheimer's disease progression. *Brain*. 2018;141:1529-1544.
12. Yan L, Liu CY, Wong KP, et al. Regional association of pCASL-MRI with FDG-PET and PiB-PET in people at risk for autosomal dominant Alzheimer's disease. *NeuroImage Clin*. 2018;17:751-760.
13. Lowe VJ, Lundt E, Knopman D, et al. Comparison of [18F]Flutemetamol and [11C]Pittsburgh Compound-B in cognitively normal young, cognitively normal elderly, and Alzheimer's disease dementia individuals. *NeuroImage Clin*. 2017;16:295-302.
14. Johnson KA, Fox NC, Sperling RA, Klunk WE. Brain imaging in Alzheimer disease. *Cold Spring Harb Perspect Med*. 2012;2:6213.
15. Choy G, Khalilzadeh O, Michalski M, et al. Current applications and future impact of machine learning in radiology. *Radiology*. 2018;288:318-328.
16. Erickson BJ, Korfiatis P, Akkus Z, Kline TL. Machine learning for Medical Imaging. *RadioGraphics*. 2017;37:505-515.
17. Passos IC, Mwangi B, Kapczynski F. Big data analytics and machine learning: 2015 and beyond. *Lancet Psychiatry*. 2016;3:13-15.
18. Ding Y, Sohn JH, Kawczynski MG, et al. A deep learning model to predict a diagnosis of Alzheimer disease by using 18F-FDG PET of the brain. *Radiology*. 2018;290:456-464.
19. Moradi E, Pepe A, Gaser C, Huttunen H, Tohka J. Machine learning framework for early MRI-based Alzheimer's conversion prediction in MCI subjects. *Neuroimage*. 2015;104:398-412.
20. Khazaee A, Ebrahimzadeh A, Babajani-Feremi A. Application of advanced machine learning methods on resting-state fMRI network for identification of mild cognitive impairment and Alzheimer's disease. *Brain Imaging Behav*. 2016;10:799-817.
21. Collij LE, Heeman F, Kuijjer JPA, et al. Application of machine learning to arterial spin labeling in mild cognitive impairment and Alzheimer Disease. *Radiology*. 2016;281:865-875.
22. Youssofzadeh V, McGuinness B, Maguire L, Wong-Lin K. Multi-kernel learning with dartel improves combined MRI-PET classification of Alzheimer's disease in AIBL data: group and individual analyses. *Front Hum Neurosci*. 2017;11:380.
23. Morris JC. The Clinical Dementia Rating (CDR): current version and scoring rules. *Neurology*. 2012;41:1588-1592.
24. Jack CR, Bernstein MA, Borowski BJ, et al. Update on the magnetic resonance imaging core of the Alzheimer's disease neuroimaging initiative. *Alzheimer's Dement*. 2010;6:212-220.
25. Fischl B. FreeSurfer. *Neuroimage*. 2012;62:774-781.
26. Fischl B, Dale AM. Measuring the thickness of the human cerebral cortex from magnetic resonance images. *Proc Natl Acad Sci U S A*. 2000;97:11050-11055.
27. Desikan RS, Ségonne F, Fischl B, et al. An automated labeling system for subdividing the human cerebral cortex on MRI scans into gyral based regions of interest. *Neuroimage*. 2006;31(3):968-980.
28. Su Y, D'Angelo GM, Vlassenko AG, et al. Quantitative analysis of PiB-PET with FreeSurfer ROIs. *PLoS One*. 2013;8:73377.
29. Su Y, Blazey TM, Snyder AZ, et al. Partial volume correction in quantitative amyloid imaging. *Neuroimage*. 2015;107:55-64.
30. Rousset OG, Ma Y, Evans AC. Correction for partial volume effects in PET: principle and validation. *J Nucl Med*. 1998;39:904-911.
31. Joshi A, Koeppe RA, Fessler JA. Reducing between scanner differences in multi-center PET studies. *Neuroimage*. 2009;46:154-159.
32. Goodfellow I, Bengio Y, Courville A. *Deep Learning*. Cambridge, MA: MIT Press; 2016.
33. Hornik K. Approximation capabilities of multilayer feedforward networks. *Neural Networks*. 1991;4:251-257.
34. Hagan MT, Demuth HB, Beale MH. *Neural Network Design*. Boston: Massachusetts PWS; 1995.
35. Heaton J. Programming neural networks in Java. *Java Dev J*; 2002.
36. Kira K, Rendell LA. A practical approach to feature selection. *Proc Ninth Int Work Mach Learn*. 1992:249-256.
37. Kotz S, Balakrishnan N, Johnson NL. *Continuous multivariate distributions, Volume 1: Models and applications: Second ed.* John Wiley & Sons, 2005.
38. Schulz M-A, Yeo BTT, Vogelstein JT, et al. Deep learning for brains? different linear and nonlinear scaling in UK Biobank brain images vs. machine-learning datasets. *BioRxiv*; 2019.
39. Jack CR, Knopman DS, Jagust WJ, et al. Hypothetical model of dynamic biomarkers of the Alzheimer's pathological cascade. *Lancet Neurol*. 2010;9:119-128.
40. Klunk WE, Price JC, Mathis CA, et al. Amyloid deposition begins in the striatum of presenilin-1 mutation carriers from two unrelated pedigrees. *J Neurosci*. 2007;27(23):6174-6184.
41. Suenaga T, Hirano A, Llena JF, Yen SH, Dickson DW. Modified Bielschowsky stain and immunohistochemical studies on striatal plaques in Alzheimer's disease. *Acta Neuropathol*. 1990;80:280-286.
42. Brilliant MJ, Elble RJ, Ghobrial M, Struble RG. The distribution of amyloid β protein deposition in the corpus striatum of patients with Alzheimer's disease. *Neuropathol Appl Neurobiol*. 1997;23:322-325.
43. Busche MA, Konnerth A. Neuronal hyperactivity - A key defect in Alzheimer's disease?. *BioEssays*. 2015;37:624-632.
44. Palop JJ, Mucke L. Epilepsy and cognitive impairments in Alzheimer disease. *Arch Neurol*. 2009;66:435-440.
45. Busche MA, Konnerth A. Impairments of neural circuit function in Alzheimer's disease. *Philos Trans R Soc B Biol Sci*. 2016;371:20150429.
46. Stargardt A, Swaab DF, Bossers K. The storm before the quiet: neuronal hyperactivity and A β in the presymptomatic stages of Alzheimer's disease. *Neurobiol Aging*. 2015;36:1-11.
47. Bero AW, Bauer AQ, Stewart FR, et al. Bidirectional relationship between functional connectivity and amyloid- β deposition in mouse brain. *J Neurosci*. 2012;32:4334-4340.
48. Wen J, Sutre ET, Samper-gonzález J, et al. How serious is data leakage in deep learning studies on Alzheimer's disease classification?. *Organ Hum Brain Mapp*. 2019.
49. Mendoza H, Klein A, Feurer M, Springenberg JT, Hutter F. Towards automatically-tuned neural networks. *Work Autom Mach Learn*. 2016.

SUPPORTING INFORMATION

Additional supporting information may be found online in the Supporting Information section at the end of the article.

How to cite this article: Lockett PH, McCullough A, Gordon BA, et al. Modeling autosomal dominant Alzheimer's disease with machine learning. *Alzheimer's Dement*. 2021;17:1005-1016. <https://doi.org/10.1002/alz.12259>

APPENDIX A

Consortia: Dominantly Inherited Alzheimer Network

Ricardo Allegri, Randall J. Bateman, Jacob Bechara, Tammie L.S. Benzinger, Sarah Berman, Courtney Bodge, Susan Brandon, William Brooks, Jill Buck, Virginia Buckles, Sochenda Chea, Jasmeer

Chhatwal, Patricio Chrem, Helena Chui, Jake Cinco, Clifford R Jack Jr, Carlos Cruchaga, Tamara Donahue, Jane Douglas, Noelia Edigo, Nilufer Erekin-Taner, Anne Fagan, Martin R. Farlow, Nick C. Fox, Colleen Fitzpatrick, Gigi Flynn, Erin Franklin, Hisako Fujii, Douglas Galasko, Cortaiga Gant, Samantha Gardener, Bernardino Ghetti, Alison Goate, Jill Goldman, Brian Gordon, Neill Graff-Radford, Julia Gray, Alexander Groves, Jason Hassenstab, Laura Hoechst-Swisher, David Holtzman, Russ Hornbeck, Siri Houeland DiBari, Takeshi Ikeuchi, Snezana Ikonovic, Gina Jerome, Mathias Jucker, Celeste Karch,

Kensaku Kasuga, Takeshi Kawarabayashi, William Klunk, Robert Koeppe, Elke Kuder-Buletta, Christoph Laske, Jae-Hong Lee, Johannes Levin, Ralph Martins, Neal Scott Mason, Ralph Martins, Colin L. Masters, Denise Maue-Dreyfus, Eric McDade, Hiroshi Mori, John C. Morris, Akem Nagamatsu, Katie Neimeyer, James M. Noble, Joanne Norton, Richard J. Perrin, Marc Raichle, Alan Renton, John Ringman, Jee Hoon Roh, Stephen Salloway, Peter R. Schofield, Hiroyuki Shimada, Wendy Sigurdson, Hamid Sohrabi, Paige Sparks, Kazushi Suzuki, Kevin Taddei, Peter Wang, Chengjie Xiong, Xiong Xu